Significance of energy conservation in coupled-trajectory approaches to non-adiabatic dynamics

Evaristo Villaseco Arribas

Department of Physics, Rutgers University, Newark 07102, New Jersey, USA and

Université Paris-Saclay, CNRS, Institut de Chimie Physique UMR8000, 91405 Orsay, France[a]

Lea M. Ibele

Université Paris-Saclay, CNRS, Institut de Chimie Physique UMR8000, 91405 Orsay, France

David Lauvergnat

Université Paris-Saclay, CNRS, Institut de Chimie Physique UMR8000, 91405 Orsay, France

Neepa T. Maitra

Department of Physics, Rutgers University, Newark 07102, New Jersey, USA[b]

Federica Agostini

Université Paris-Saclay, CNRS, Institut de Chimie Physique UMR8000, 91405 Orsay, France[c]

Through approximating electron-nuclear correlation terms in the exact factorization approach, trajectory-based methods have been derived and successfully applied to the dynamics of a variety of light-induced molecular processes, capturing quantum (de)coherence effects rigorously. These terms account for the coupling among the trajectories, recovering the non-local nature of quantum nuclear dynamics which is completely overlooked in traditional independent-trajectory algorithms. Nevertheless, some of the approximations introduced in the derivation of some of these methods do not conserve the total energy. We analyze energy conservation in the coupled-trajectory mixed quantum-classical (CTMQC) algorithm and explore the performance of a modified algorithm, CTMQC-E where some of the terms are redefined to restore energy conservation. A set of molecular models is used as test, namely 2-cis-penta-2,4-dienimium cation, bis(methylene) adamantyl radical cation, butatriene cation, uracil radical cation, and neutral pyrazine.

---

[a]Electronic mail: evaristo.villaseco@rutgers.edu

[b]Electronic mail: neepa.maitra@rutgers.edu

[c]Electronic mail: federica.agostini@universite-paris-saclay.fr

I. INTRODUCTION

The accurate description of non-adiabatic processes where the electronic and nuclear motion is highly correlated is fundamental to our understanding of a wide variety of phenomena ranging from photosynthesis[1–3], DNA photo-damage[4–6] or charge transfer in photo-voltaic cells[7–9]. The full quantum-mechanical treatment of the dynamics beyond the Born-Oppenheimer approximation[10] remains limited to a few degrees of freedom and approximate methods that treat the nuclei quantum-mechanically become unfeasible for large systems without a heavy investment in computational resources, or recent cutting-edge technologies[11]. Justified by the large nuclear-electron mass ratio, trajectory-based schemes are the basis for many approximations for coupled electron-nuclear dynamics, where one propagates an ensemble of classical-like nuclear trajectories, each associated with a set of quantum electronic coefficients of, typically, a Born-Huang basis. The methods stem from a quantum evolution equation such as the time-dependent Schrödinger equation in the conventional Born-Huang picture[12–14], the exact factorization equations[15–18] or the Liouville equation[19–23]. In those frameworks, the classical limit for the nuclear motion is taken, while the electronic degrees of freedom are kept quantum-mechanical. Different trajectory-based schemes involve different approximations, and as a result of those approximations some exact physical constraints might be broken. One important example is the conservation of total energy which is a manifestation of the symmetry of the system under time-translation. Specifically, in the full quantum-mechanical picture the expectation value of the molecular Hamiltonian over the total molecular wavefunction is a constant of motion when no external fields are present. In the approximate trajectory-based view, energy can be exchanged between the ensemble of classical (nuclei) and quantum (electrons) degrees of freedom but should be such that the total energy of the system remains invariant. The most widely used trajectory-based methods, Ehrenfest dynamics and surface-hopping[13,24], impose this conservation law although in a somewhat restrictive way: each individual trajectory in the ensemble conserves its classical energy in these schemes but it is the energy of the trajectory ensemble as a whole that should be conserved, as it is the ensemble that represents the nuclear wavepacket. In principle, trajectories should be able to exchange energy, but this is not possible with independent trajectory schemes such as these. This tight constraint on the energy conservation of the system might prevent opening channels for the classical trajectories in the energy landscape that are accessible in the quantum dynamics, leading to inaccuracies. Further, the disconnect between coherent electronic evolution and incoherent nuclear trajectory propagation in surface-hopping means that energy is only conserved when the potential energy of the system is defined in terms of the instantaneous active state energy rather than from the coherent electronic evolution. This will be further discussed in the next section.

While the exact factorization[25–34] has offered a new framework to develop new trajectory-based methods, capturing quantum (de)coherence effects in a variety of photochemically interesting systems from first principles, these methods are not immune to the breakdown of physical constraints such as energy conservation due to approximations made in their derivation. The coupled-trajectory mixed quantum-classical (CTMQC) algorithm was the method that was derived first and, at its core, consists of an ensemble of classical-like trajectories that are coupled throughout their dynamics. Such coupling provides new mechanisms to

2

correctly reproduce quantum (de)coherence effects. A modification in the algorithm was recently proposed, dubbed CTMQC-E, which restores energy conservation for the ensemble of coupled trajectories[35]. In this work, we extensively analyze the extent and implications of energy (non)conservation in CTMQC and in CTMQC-E with a detailed study of electronic and nuclear properties for a variety of molecular models parametrized to reproduce the dynamics of a set of molecules with different features, e.g. different topologies of conical intersections and of growing complexity. We study the ultrafast dynamics through a 2-dimensional conical intersection in bis(methylene)adamantyl (BMA) radical cation, butatriene cation and pyrazine, the photoisomerization dynamics of 2-cis-penta-2,4-dieniminium cation (PSB3) and the photo-relaxation dynamics after photo-ionization through a 3-states conical intersection in the uracil radical cation.

The paper is organized as follows. In Section II we begin first by reviewing the exact factorization approach and the trajectory-based methods derived from it, then examine energy conservation in these methods and introduce the modified CTMQC-E algorithm. Section III is devoted to numerical simulations of the molecular models comparing the performance of CTMQC-E with respect to CTMQC as well as surface-hopping with energy-based decoherence correction. Section IV at last provides the main conclusions of our work as well as an outlook.

II. THEORETICAL BACKGROUND

A. The Exact Factorization Approach

Let's briefly review the exact factorization (EF) equations. In the EF, the full molecular wavefunction is factorized into a single correlated product[31,32]

$$\Psi(\underline{\mathbf{r}}, \underline{\mathbf{R}}, t) = \chi(\underline{\mathbf{R}}, t)\phi_{\underline{\mathbf{R}}}(\underline{\mathbf{r}}, t) \tag{1}$$

where variables $\underline{\mathbf{r}}$, $\underline{\mathbf{R}}$ denote all the electronic and nuclear coordinates respectively. The time evolution of the electronic ($\phi_{\underline{\mathbf{R}}}(\underline{\mathbf{r}}, t)$) and nuclear ($\chi(\underline{\mathbf{R}}, t)$) subsystems are governed by a set of coupled equations

$$i\partial_t \Phi_{\underline{\mathbf{R}}}(\underline{\mathbf{r}}, t) = \left(\hat{H}_{el}(\underline{\mathbf{r}}, \underline{\mathbf{R}}, t) - \varepsilon(\underline{\mathbf{R}}, t)\right)\Phi_{\underline{\mathbf{R}}}(\underline{\mathbf{r}}, t) \tag{2}$$

$$i\partial_t \chi(\underline{\mathbf{R}}, t) = \left(\hat{\bar{T}}_N(\underline{\mathbf{R}}, t) + \varepsilon(\underline{\mathbf{R}}, t)\right)\chi(\underline{\mathbf{R}}, t) \tag{3}$$

with the electronic Hamiltonian $\hat{H}_{el}$ and the mechanical nuclear kinetic energy operators. Note that we name the operator $\hat{\bar{T}}_N(\underline{\mathbf{R}}, t)$ mechanical kinetic energy operator in analogy with the mechanical momentum $\tilde{\mathbf{p}}_\nu = m\mathbf{v}_\nu = \mathbf{p}_\nu - \mathbf{A}_\nu$ in the presence of an electromagnetic field with $\mathbf{p}_\nu = -i\nabla_\nu$ being the canonical momentum operator that satisfies the commutation relations $[p_{\nu,i}, R_{\nu,j}] = i\delta_{ij}$ for $i = x, y, z$. $\hat{\bar{T}}_N$ is defined as

$$\hat{H}_{el}(\underline{\mathbf{r}}, \underline{\mathbf{R}}, t) = \hat{H}_{BO}(\underline{\mathbf{r}}, \underline{\mathbf{R}}) + \hat{U}_{en}[\Phi_{\underline{\mathbf{R}}}, \chi] \tag{4}$$

$$\hat{\bar{T}}_N(\underline{\mathbf{R}}, t) = \sum_{\nu=1}^{N_n} \frac{1}{2M_\nu}(-i\nabla_\nu + \mathbf{A}_\nu(\underline{\mathbf{R}}, t))^2 \tag{5}$$

3

Atomic units are used throughout this article. Nuclear masses are indicated with the symbol M_ν, with ν labelling the N_n nuclei. $\hat{H}_{BO}$ is the Born-Oppenheimer (BO) Hamiltonian (the sum of the electron kinetic energy, electron-electron, nuclear-nuclear, and electron-nuclear interaction operators). The electron-nuclear coupling term reads

$$\hat{U}_{eN}[\Phi_{\underline{\underline{R}}}, \chi] = \sum_{\nu=1}^{N_n} \frac{1}{M_\nu} \left[\frac{(-i\nabla_\nu - \mathbf{A}_\nu(\underline{\underline{R}}, t))^2}{2} \right.$$
$$\left. + \left(\frac{-i\nabla_\nu \chi(\underline{\underline{R}}, t)}{\chi(\underline{\underline{R}}, t)} + \mathbf{A}_\nu(\underline{\underline{R}}, t) \right) \left(-i\nabla_\nu - \mathbf{A}_\nu(\underline{\underline{R}}, t) \right) \right] \tag{6}$$

and the time-dependent potential energy surface (TDPES) is

$$\varepsilon(\underline{\underline{R}}, t) = \left\langle \Phi_{\underline{\underline{R}}}(t) \left| \hat{H}_{el}(\underline{\underline{R}}, t) - i\partial_t \right| \Phi_{\underline{\underline{R}}}(t) \right\rangle_{\underline{\underline{r}}} \tag{7}$$

Together with the time-dependent vector potential appearing in Eqs. (2) and (6)

$$\mathbf{A}_\nu(\underline{\underline{R}}, t) = \left\langle \Phi_{\underline{\underline{R}}}(t) \left| -i\nabla_\nu \Phi_{\underline{\underline{R}}}(t) \right\rangle_{\underline{\underline{r}}} \right. , \tag{8}$$

these three terms capture exactly electron-nuclear correlation. The symbol $\langle ... \rangle_{\underline{\underline{r}}}$ stands for an integration over the electronic variables. In this framework, the total energy of the molecule can be written as

$$\langle E \rangle = \langle \Psi(t) | \hat{H}_{BO} + \hat{T}_N | \Psi(t) \rangle_{\underline{\underline{r}}, \underline{\underline{R}}} \tag{9}$$

The nuclear kinetic energy can be written as a sum of two contributions[32,36,37]

$$\langle \hat{T}_N \rangle_{\underline{\underline{r}}, \underline{\underline{R}}} = \langle \chi(t) | \hat{\bar{T}}_N | \chi(t) \rangle_{\underline{\underline{R}}} + T_{N,geom} \tag{10}$$

where the first term stands for the expectation value of $\hat{\bar{T}}_N$ over the nuclear wavefunction only, and second term is a geometric term which can be expressed as the nuclear-density-weighted integral of the electron-nuclear coupling operator

$$T_{N,geom} = \int d\underline{\underline{R}} |\chi(\underline{\underline{R}}, t)|^2 \langle \Phi_{\underline{\underline{R}}} | \hat{U}_{eN} | \Phi_{\underline{\underline{R}}} \rangle_{\underline{\underline{r}}} \tag{11}$$

This geometric term accounts for difference between the nuclear kinetic energy evaluated from the full molecular wavefunction and that evaluated as the expectation value of the mechanical nuclear kinetic energy operator on the nuclear wavefunction.

B.   Exact-Factorization based mixed quantum-classical methods

CTMQC[15,16] was derived by taking the classical limit of the nuclear motion, expanding the time-dependent electronic wavefunction in the Born-Huang (BH) basis

$$\phi_{\underline{\underline{R}}}(\underline{\underline{r}}, t) = \sum_l C_l(\underline{\underline{R}}, t) \phi_{\underline{\underline{R}}}^l(\underline{\underline{r}}) \tag{12}$$

4

and neglecting some terms in the equations based on exact studies[38,39]. Let us briefly review the CTMQC equations. The electronic coefficients evolve as

$$\dot{C}_l^{(\alpha)}(t) = \dot{C}_{l,Eh}^{(\alpha)}(t) + \dot{C}_{l,CT}^{(\alpha)}(t) \tag{13}$$

and the nuclear force is given by

$$\mathbf{F}_\nu^{(\alpha)}(t) = \mathbf{F}_{\nu,Eh}^{(\alpha)}(t) + \mathbf{F}_{\nu,CT}^{(\alpha)}(t) \tag{14}$$

where the first terms in both equations are Ehrenfest-like terms:

$$\dot{C}_{l,Eh}^{(\alpha)} = -i\epsilon_l^{(\alpha)} C_l^{(\alpha)} - \sum_k \sum_\nu^{N_n} \dot{\mathbf{R}}_\nu^{(\alpha)} \cdot \mathbf{d}_{\nu,lk}^{(\alpha)} C_k^{(\alpha)} \tag{15}$$

$$\mathbf{F}_{\nu,Eh}^{(\alpha)} = -\sum_l \rho_{ll}^{(\alpha)} \nabla_\nu \epsilon_l^{(\alpha)} + \sum_{l,k} \rho_{lk}^{(\alpha)} \Delta\epsilon_{lk}^{(\alpha)} \mathbf{d}_{\nu,lk}^{(\alpha)} \tag{16}$$

We have adopted the shorthand notation $f^{(\alpha)} = f(\underline{\underline{\mathbf{R}}}^{(\alpha)}(t))$ denoting evaluation of a function f of the nuclear coordinates at the position of trajectory α. From this point forward we omit the t-dependences of the quantities to avoid notational clutter. The electronic density-matrix elements are $\rho_{lk}^{(\alpha)} = C_l^{(\alpha)*} C_k^{(\alpha)}$, $\mathbf{d}_{\nu,lk}^{(\alpha)}$ is the nonadiabatic coupling (NAC) vector along the ν nuclear coordinate between BO states l and k, i.e. $\langle \phi_{\underline{\underline{\mathbf{R}}}}^l(\underline{\mathbf{r}}) | \nabla_\nu \phi_{\underline{\underline{\mathbf{R}}}}^k(\underline{\mathbf{r}}) \rangle |_{\underline{\underline{\mathbf{R}}}^{(\alpha)}}$; the sums over Latin indices go over the electronic states. The eigenvalues of $\hat{H}_{BO}$, i.e. the adiabatic or BO potential energy surfaces (PES), are denoted $\epsilon_l^{(\alpha)}$ and $\Delta\epsilon_{lk}^{(\alpha)}$ is the energy difference between states l and k at the nuclear configuration $\underline{\underline{\mathbf{R}}}^{(\alpha)}(t)$. The second terms in Eqs (13) and (14) are the corrections arising from EF

$$\dot{C}_{l,CT}^{(\alpha)} = \sum_\nu^{N_n} \sum_k \frac{\mathbf{Q}_\nu^{(\alpha)}}{M_\nu} \cdot \Delta\mathbf{f}_{\nu,lk}^{(\alpha)} \rho_{kk}^{(\alpha)} C_l^{(\alpha)} \tag{17}$$

$$\mathbf{F}_{\nu,CT}^{(\alpha)}(t) = \sum_\mu^{N_n} \sum_{l,k} \frac{2\mathbf{Q}_\mu^{(\alpha)}}{M_\mu} \cdot \mathbf{f}_{\mu,l}^{(\alpha)} \rho_{ll}^{(\alpha)} \rho_{kk}^{(\alpha)} \Delta\mathbf{f}_{\nu,lk}^{(\alpha)} \tag{18}$$

with subscript CT used to denote that these terms involve coupled trajectories. $\Delta\mathbf{f}_{\nu,lk}^{(\alpha)} = \mathbf{f}_{\nu,l}^{(\alpha)} - \mathbf{f}_{\nu,k}^{(\alpha)}$, where $\mathbf{f}_{\nu,l}^{(\alpha)}$ is the time-integrated adiabatic force on nucleus ν accumulated on the l-th BO PES along the trajectory α (i.e. an adiabatic momentum)

$$\mathbf{f}_{\nu,l}^{(\alpha)} = -\int_0^t \nabla_\nu \epsilon_l^{(\alpha)} d\tau, \tag{19}$$

and $\mathbf{Q}_\nu^{(\alpha)}$ is the nuclear quantum momentum evaluated at the position of the trajectory $\underline{\underline{\mathbf{R}}}^{(\alpha)}(t)$

$$\mathbf{Q}_\nu^{(\alpha)} = -\frac{\nabla_\nu |\chi^{(\alpha)}|^2}{2|\chi^{(\alpha)}|^2} \tag{20}$$

Variations of the CTMQC algorithm have been explored, for example, using the electronic equation Eq.(13) within a surface-hopping (SH) or Ehrenfest (Eh) scheme for the nuclear

5

evolution[18,40–42], resulting in a family of trajectory-based methods. A central feature of these methods is the coupling of trajectories through the nuclear quantum momentum Eq. (20) appearing in the EF terms. This term can be computed in two different ways. The original definition ($\mathbf{Q}_0$) implies using Eq.(20) where the nuclear density is reconstructed as a sum of gaussians centered at the position of the classical trajectories or by placing the gaussian functions on auxiliary trajectories[41] created on non-active BO PES to approximate this coupling locally. This definition potentially leads to unphysical spurious net electronic population transfer in regions of zero NAC[16,17,43]. To circumvent this problem, the quantum momentum is redefined ($\mathbf{Q}_m$) by imposing, per degree of freedom, zero net population transfer between each pair of electronic states coming from the CT term[16,17]

$$\sum_{\alpha}^{N_{tr}} \frac{Q_{\mu,i,lk}^{(\alpha)}}{M_\mu} \rho_{ll}^{(\alpha)} \rho_{kk}^{(\alpha)} \Delta f_{\mu,i,lk}^{(\alpha)} = 0 \qquad i = x, y, z \tag{21}$$

Note that even though the trajectory-averaged population-transfer coming from the CT term is zero, the quantum momentum can induce population transfer associated with an individual trajectory, a mechanism that is lacking in traditional methods[34]. The modified definition of the quantum momentum ($\mathbf{Q}_m$) resulting from Eq. (21) has been successfully applied in CTMQC calculations of photo-induced molecular dynamics[17,44–47]. This condition of zero net population transfer in regions of zero NAC may be viewed as an exact condition to be imposed within the algorithm, as we will shortly do for the conservation of total energy[35].

C.   Energy conservation in trajectory-based methods

Let us start by reviewing energy conservation in standard trajectory-based schemes, i.e. Eh and SH. Both treat the nuclear degrees of freedom classically, therefore the nuclear kinetic energy term simply reduces to the classical kinetic energy of the nuclei

$$\hat{T}_N = -\sum_\nu \frac{1}{2M_\nu} \nabla_\nu^2 \rightarrow T_N^{(\alpha)} = \sum_\nu -\frac{1}{2} M_\nu \dot{\mathbf{R}}_\nu^{(\alpha)\,2} \tag{22}$$

which would then be ensemble-averaged. In Eh dynamics the effective potential energy, $U^{(\alpha)}$, of the system along the α-th trajectory is the expectation value of the time-independent electronic Hamiltonian over the instantaneous electronic wavefunction along that trajectory:

$$U^{(\alpha)} = \langle \Phi^{(\alpha)} | \hat{H}_{BO} | \Phi^{(\alpha)} \rangle_{\underline{\mathbf{r}}} = \sum_l \rho_{ll}^{(\alpha)} \epsilon_l^{(\alpha)} \tag{23}$$

This effective potential, when used in conjunction with the mean-field force acting on the nuclei $M_\nu \ddot{\mathbf{R}}_\nu^{(\alpha)} = -\langle \Phi^{(\alpha)} | \nabla_\nu \hat{H}_{BO} | \Phi^{(\alpha)} \rangle = \mathbf{F}_{\nu,Eh}^{(\alpha)}$ given by Eq. (16), results in the time-derivative of the total energy along a trajectory

$$\frac{dE^{(\alpha)}}{dt} = \frac{dT_N^{(\alpha)}}{dt} + \frac{dU^{(\alpha)}}{dt} = \frac{dT_N^{(\alpha)}}{dt} + \partial_t U^{(\alpha)} + \sum_\nu \nabla_\nu U^{(\alpha)} \cdot \dot{\mathbf{R}}_\nu^{(\alpha)}$$

$$= \sum_\nu \mathbf{F}_{\nu,Eh}^{(\alpha)} \cdot \dot{\mathbf{R}}_\nu^{(\alpha)} + \sum_l^{N_{st}} \dot{\rho}_{ll,Eh}^{(\alpha)} \epsilon_l^{(\alpha)} + \sum_l \rho_{ll}^{(\alpha)} \sum_\nu \left(\nabla_\nu \epsilon_l^{(\alpha)} \right) \cdot \dot{\mathbf{R}}_\nu^{(\alpha)} = 0 \tag{24}$$

6

which by inserting Eqs. (15-16), can be shown to be zero, implying energy conservation.

In the case of SH, energy conservation is more subtle. This stems from the inconsistency of having a coherent electronic evolution while each nuclear trajectory is collapsed on a given surface at any time. The potential that drives the nuclear motion is the instantaneous active state BO energy, i.e, $M_\nu \dot{\mathbf{R}}_\nu^{(\alpha)} = -\nabla_\nu \epsilon_{active}^{(\alpha)}$. If the electronic potential energy is determined from the quantum-mechanical electronic populations along a trajectory then the potential energy is given by Eq. (23), and energy is not conserved since $\mathbf{F}_\nu^{(\alpha)} \cdot \dot{\mathbf{R}}_\nu^{(\alpha)} = -\nabla_\nu \epsilon_{active}^{(\alpha)} \cdot \dot{\mathbf{R}}_\nu^{(\alpha)} \neq \nabla_\nu U^{(\alpha)} \cdot \dot{\mathbf{R}}_\nu^{(\alpha)} + \partial_t U^{(\alpha)}$. However if instead the electronic populations in the definition of the energy are obtained from the fraction of trajectories, i.e. $\rho_{ll}^{(\alpha)} \to \delta_{l,active}^{(\alpha)}$, then we would define the potential energy through

$$U^{(\alpha)} = \epsilon_{active}^{(\alpha)} \tag{25}$$

and each trajectory in the ensemble conserves total energy. Further, when a hop occurs the velocity of the trajectory can be rescaled in different ways[48–50] to satisfy energy conservation.

Let us now analyze energy conservation in EF trajectory-based schemes. We start by defining the total energy of the molecule from the expectation value of the full Hamiltonian over the factorized wavefunction

$$\langle E \rangle = \langle \Psi | \hat{H}_{BO} | \Psi \rangle_{\mathbf{r},\underline{\underline{\mathbf{R}}}} + \langle \chi | \hat{\bar{T}}_N | \chi \rangle_{\underline{\underline{\mathbf{R}}}} + T_{N,geom} \tag{26}$$

The geometric contribution to the kinetic energy will be set to zero to be consistent with the neglect of $\hat{U}_{eN}$ within CTMQC. To analyze the marginal kinetic term, we write the nuclear wavefunction in its polar representation $\chi(\underline{\underline{\mathbf{R}}}, t) = |\chi(\underline{\underline{\mathbf{R}}}, t)|e^{iS(\underline{\underline{\mathbf{R}}},t)}$ such that

$$\langle \chi | \hat{\bar{T}}_N | \chi \rangle_{\underline{\underline{\mathbf{R}}}} = \int d\underline{\underline{\mathbf{R}}} |\chi(\underline{\underline{\mathbf{R}}}, t)|^2 \left[\sum_\nu \frac{1}{2M_\nu} \left(\nabla_\nu S(\underline{\underline{\mathbf{R}}}, t) + \mathbf{A}_\nu(\underline{\underline{\mathbf{R}}}, t) \right)^2 + \mathcal{Q}(\underline{\underline{\mathbf{R}}}, t) \right] \tag{27}$$

where we can identify the mechanical momentum $M_\nu \dot{\mathbf{R}}_\nu = \nabla_\nu S(\underline{\underline{\mathbf{R}}}, t) + \mathbf{A}_\nu(\underline{\underline{\mathbf{R}}}, t)$ and the quantum potential

$$\mathcal{Q}(\underline{\underline{\mathbf{R}}}, t) = -\sum_\nu \frac{1}{2M_\nu} \frac{\nabla_\nu^2 |\chi(\underline{\underline{\mathbf{R}}}, t)|}{|\chi(\underline{\underline{\mathbf{R}}}, t)|} . \tag{28}$$

Since the quantum potential is neglected in deriving the CTMQC equations of motion for the trajectories[15,16], we neglect it in the expression of the energy for consistency. Writing the electronic wavefunction in a BH-like expansion, i.e Eq. (12), and reconstructing the nuclear density from the classical distribution of point-like trajectories

$$|\chi(\underline{\underline{\mathbf{R}}}, t)|^2 = \frac{1}{N_{tr}} \sum_\alpha^{N_{tr}} \delta(\underline{\underline{\mathbf{R}}} - \underline{\underline{\mathbf{R}}}^{(\alpha)}(t)) \tag{29}$$

we derive[51]

$$\langle E \rangle = \frac{1}{N_{tr}} \sum_\alpha^{N_{tr}} \left(\frac{1}{2} \sum_\nu^{N_n} M_\nu \dot{\mathbf{R}}_\nu^{(\alpha)2} + \sum_l \rho_{ll}^{(\alpha)} \epsilon_l^{(\alpha)} \right) \tag{30}$$

7

Thus the time-derivative of the CTMQC energy yields

$$\langle \dot{E} \rangle = \frac{1}{N_{tr}} \sum_{\alpha}^{N_{tr}} \left(\sum_{\nu} \mathbf{F}_{\nu,CT}^{(\alpha)} \cdot \dot{\mathbf{R}}_{\nu}^{(\alpha)} + \sum_{l}^{N_{st}} \dot{\rho}_{ll,CT}^{(\alpha)} \epsilon_l^{(\alpha)} \right)$$

$$= \frac{1}{N_{tr}} \sum_{\alpha}^{N_{tr}} \sum_{\mu} \frac{\mathbf{Q}_{\mu}^{(\alpha)}}{M_{\mu}} \cdot \sum_{l,k} \rho_{ll}^{(\alpha)} \rho_{kk}^{(\alpha)} \Delta \mathbf{f}_{\mu,lk}^{(\alpha)} \left[\sum_{\nu} \Delta \mathbf{f}_{\nu,lk}^{(\alpha)} \cdot \dot{\mathbf{R}}_{\nu}^{(\alpha)} + \Delta \epsilon_{lk}^{(\alpha)} \right] \quad (31)$$

which shows that, in general, energy-conservation is not guaranteed in this scheme. It should be noted that total energy conservation is also not assured in the other members of the family of EF trajectory-based methods. MQCXF uses the same electronic evolution and nuclear force as in CTMQC using auxiliary trajectories to compute the quantum momentum, and thus it does not satisfy energy conservation[41]. CTTSH[40] and SHXF[18] use the electronic equation Eq.(13) within a SH framework, and as we discussed previously, the total energy of each trajectory will only be conserved if the electronic populations in the definition of the energy are obtained from the fraction of trajectories. On the other hand, CTEh and EhXF use the electronic equation Eq.(13) with an Eh force acting on the nuclei, and as we can see from Eq.(31) this implies energy non-conservation $\langle \dot{E} \rangle = \frac{1}{N_{tr}} \sum_{\alpha}^{N_{tr}} \sum_{l}^{N_{st}} \dot{\rho}_{ll,CT}^{(\alpha)} \epsilon_l^{(\alpha)}$.

D.   The CTMQC-E algorithm

As we mentioned in section II B, the quantum momentum is redefined in CTMQC to satisfy an exact condition of zero net population transfer in regions of zero NAC[16,17]. In the same spirit, some of us recently proposed a modification to CTMQC, named the CTMQC-E algorithm[35], where an exact constraint, namely total energy conservation, is imposed by redefining the time-integrated adiabatic force $\mathbf{f}_{\mu,l}^{(\alpha)}$. This approach was inspired by the work of Min and coworkers[41] which fixed energy conservation along each trajectory in the independent trajectory version of CTMQC that uses auxiliary trajectories to evaluate the quantum momentum. Instead CTMQC-E preserves the coupled-trajectory nature of CTMQC and allows the trajectories to exchange energy. It is the total energy of the *ensemble* rather than the energy of each trajectory, that is the conserved quantity. In the framework of the modified definition of the quantum momentum Eq. (21), we see from Eq. (31) that energy will be conserved in situations where the quantity in the square brackets, $\sum_{\nu} \Delta \mathbf{f}_{\nu,lk}^{(\alpha)} \cdot \dot{\mathbf{R}}_{\nu}^{(\alpha)} + \Delta \epsilon_{lk}^{(\alpha)}$ is independent of the trajectory index. CTMQC-E enforces this by redefining the accumulated force $\mathbf{f}_{\nu,l}^{(\beta)} \to \tilde{\mathbf{f}}_{\nu,l}^{(\beta)}$ in such a way that such term equals its trajectory average, namely

$$\sum_{\nu} \tilde{\mathbf{f}}_{\nu,l}^{(\beta)} \cdot \dot{\mathbf{R}}_{\nu}^{(\beta)} + \Delta \epsilon_{lk}^{(\beta)} = \frac{1}{N_{tr}} \left(\sum_{\alpha,\nu} \mathbf{f}_{\nu,l}^{(\alpha)} \cdot \dot{\mathbf{R}}_{\nu}^{(\alpha)} + \Delta \epsilon_{lk}^{(\alpha)} \right) \quad (32)$$

It automatically follows from Eq. (31) that $\langle \dot{E} \rangle = 0$. A solution that satisfies Eq. (32) is:

$$\tilde{\mathbf{f}}_{\nu,l}^{(\beta)} = \frac{\left(-\epsilon_l^{(\beta)} + \frac{1}{N_{tr}} \sum_{\alpha,\nu} \mathbf{f}_{\nu,l}^{(\alpha)} \cdot \dot{\mathbf{R}}_{\nu}^{(\alpha)} + \epsilon_l^{(\alpha)} \right)}{\sum_{\mu} \mathbf{n}_{\mu}^{(\beta)} \cdot \dot{\mathbf{R}}_{\mu}^{(\beta)}} \mathbf{n}_{\nu}^{(\beta)} \quad (33)$$

8

	M	N_{dof}	T	ΔE (CTMQC)	ΔE (CTMQC-E)	%E
BMA	2.0	2	24	0.1000	0.0090	91.00
Butatriene	2.0	2	48	1.6142	0.4040	74.97
Pyrazine	2.0	2	100	2.1611	0.2656	87.70
PSB3	53482.8	3	180	2.5556	0.3486	86.34
Uracil cation	204321.67	8	60	2.2597	0.9003	60.16

TABLE I. Total mass (M) in atomic units, number of degrees of freedom (N_{dof}), total simulation time (T) in fs, total energy deviation (ΔE) in eV and reduction in % of energy deviation of CTMQC-E with respect to CTMQC for the studied models.

where $\mathbf{n}_\nu^{(\beta)}$ is an arbitrary vector defining the direction of $\tilde{\mathbf{f}}_{\nu,I}^{(\beta)}$. While any direction for $\mathbf{n}_\nu^{(\beta)}$ in Eq. (33) guarantees energy conservation, we choose $\mathbf{n}_\nu^{(\beta)}$ as the instantaneous mechanical momentum of the trajectory $\mathbf{n}_\nu^{(\beta)} = M_\nu \dot{\mathbf{R}}_\nu^{(\beta)}$, with the reasoning that the accumulated force, Eq. (19), represents a momentum along the trajectory

$$\tilde{\mathbf{f}}_{\nu,I}^{(\beta)} = \frac{\left(-\epsilon_I^{(\beta)} + \frac{1}{N_{tr}}\sum_{\alpha\nu}\mathbf{f}_{\nu,I}^{(\alpha)}\cdot\dot{\mathbf{R}}_\nu^{(\alpha)} + \epsilon_I^{(\alpha)}\right)}{2E_{kin}^{(\beta)}/M_\nu}\dot{\mathbf{R}}_\nu^{(\beta)} \tag{34}$$

The choice of this direction results in the EF-contribution to the nuclear force in Eq. (18) being parallel to the trajectory's momentum. The correction to the accumulated force in Eq. (34) to the CTMQC algorithm, namely CTMQC-E, is currently implemented in the G-CTMQC package[52] and can be freely accessed on GitLab under GNU Lesser General Public License (LGPL).

III.   NUMERICAL SIMULATIONS

In this section, we present studies of nonadiabatic dynamics in different molecular models exploring the performance of CTMQC-E imposing energy conservation when CTMQC fails doing so. Our main findings are summarized in Table I. In the table we report the name of the molecular model that will be presented in the first column, i.e. BMA, butatriene cation and pyrazine (section III A), PSB3 (section III B) and uracil radical cation (section III C). The following columns are the total nuclear masses, the number of the nuclear degrees of freedom and the length of the simulations. Over those propagation times we observe a certain deviation (ΔE) of the total energy for a CTMQC dynamics which is strongly reduced by CTMQC-E. To quantify the improvement of the energy conservation we compute $(\Delta E(\text{CTMQC}) - \Delta E(\text{CTMQC}-\text{E})/\Delta E(\text{CTMQC})$ to estimate the relative improvement of CTMQC-E over CTMQC, which is given in the last column of the table. In the following sections, we will give an overview of various observables affected by the correction proposed in CTMQC-E.

A.   Dynamics through a 2D-CI in BMA, Butatriene cation and Pyrazine

Our first example is a set of 2-dimensional 2-state linear vibronic coupling models[53] which represent molecular systems with a conical intersection (CI): bis(methylene) adamantyl

9

(BMA) radical cation , butatriene cation and pyrazine. The dynamics through the CIs in these systems was studied with ab initio multiple spawning (AIMS) and SH in Ref. [54], where both AIMS and SH performed well in describing the dynamics through the CI in these systems. It is has been argued[53] that the lack of geometric phase effects in methods such as AIMS (SPA0) and SH is compensated by their neglect of the diagonal BO corrections.

We will test the performance of CTMQC-E, with respect to CTMQC and SH with energy decoherence correction[55] (SH-EDC) having quantum dynamical results as benchmark.
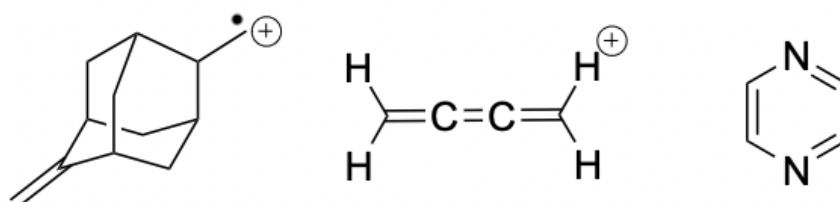
FIG. 1. Lewis structures of BMA, butatriene cation and pyrazine.

The BO Hamiltonian for these systems is modelled in the diabatic basis by

$$H_{BO}(x, y) = \begin{pmatrix} V_1(x, y) & \lambda(y) \\ \lambda(y) & V_2(x, y) \end{pmatrix} \tag{35}$$

where the diabatic potentials $V_1(x, y)$ and $V_2(x, y)$ are two identical two-dimensional harmonic oscillators with centers shifted with respect to one another in the x direction and displaced in energy. They are coupled through a linear potential $\lambda(y)$ in the y-direction. Figure 2 shows the adiabatic PESs obtained from diagonalizing Eq. (35) for the BMA model. The details of the models can be found in appendix A1. For the quantum dynamics (QD) simulations, the time-dependent Schrödinger equation is solved on a grid in the diabatic basis using the split-operator method[56,57]. The initial gaussian nuclear wavepacket is initialized in the excited adiabatic state $\chi_{S_1}(x, y, 0) = \mathcal{N}e^{-\left(\frac{x-x_0}{\sigma_x}\right)^2} e^{-\left(\frac{y-y_0}{\sigma_y}\right)^2}$ with widths, in bohr, of $\sigma_x = \sqrt{\frac{2}{\omega_1}}$ and $\sigma_y = \sqrt{\frac{2}{\omega_2}}$. This yields to widths of $(16.07, 17.30)$ bohr for BMA, $(14.47, 24.43)$ bohr for butatriene cation and $(23.41, 21.86)$ bohr for pyrazine. The centers of the wavepacket correspond to the Franck-Condon point of the ground state of the full dimensional model, i.e., $(15.53, 0.0)$ bohr for BMA, $(-2.08, 0.0)$ bohr for butatriene cation and $(5.10, 0.0)$ bohr for pyrazine. For the trajectory-based simulations $N_{tr} = 1000$ Wigner-distributed trajectories are run starting on the excited state and the time-step used in the calculations is $dt = 0.0024$ fs $(0.1\hbar/\text{Ha})$. For SH-EDC the value for the C parameter that determines the decoherence rate was chosen to be $C = 0.1$ Ha. The populations and coherences in the QD simulations are obtained via numerical integration

$$P_l^{QD}(t) = \int \int dx dy \ |\chi_l(x, y, t)|^2$$
$$\sigma_{lk}^{QD}(t) = \int \int dx dy \ \frac{|\chi_l(x, y, t)|^2 |\chi_k(x, y, t)|^2}{|\chi(x, y, t)|^2} \tag{36}$$
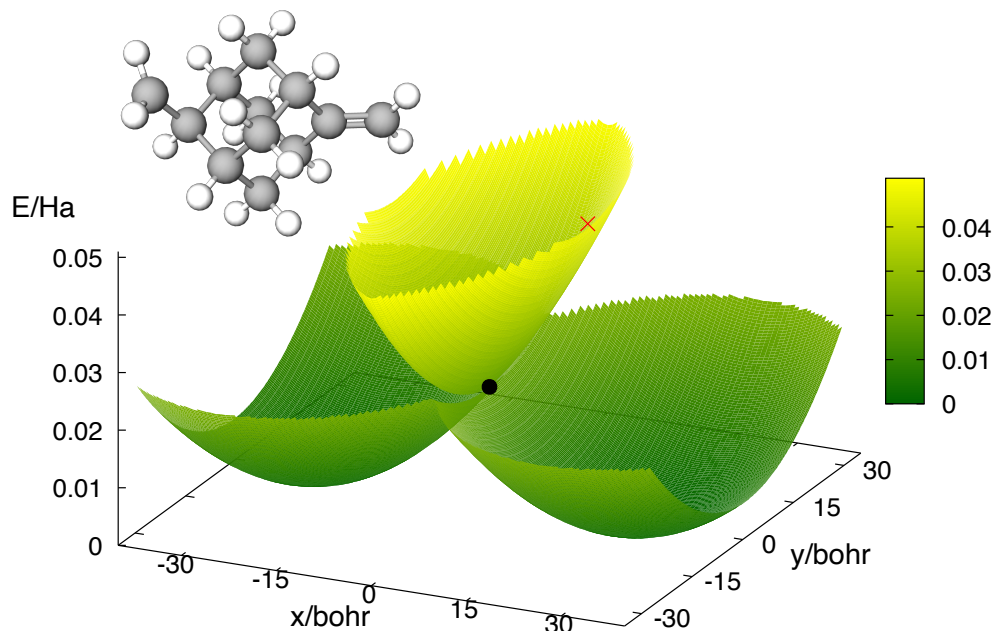
10

FIG. 2. Adiabatic PESs for the BMA molecular model. The black dot indicate the location of the conical intersection, and the red cross the center of the initial Gaussian nuclear wavepacket.

where $\{\chi_l(x, y, t)\}$ are the nuclear-coordinate and time-dependent coefficients in the BH expansion of the full state of the system and $|\chi(x, y, t)|^2 = \sum_l |\chi_l(x, y, t)|^2$ is the total nuclear density. The trajectory-based (quantum-classical) analogous quantities are ensemble-averages

$$P_l^{QC}(t) = \frac{1}{N_{tr}} \sum_{\alpha}^{N_{tr}} \rho_{ll}^{(\alpha)}(t)$$

$$\sigma_{lk}^{QC}(t) = \frac{1}{N_{tr}} \sum_{\alpha}^{N_{tr}} |\rho_{lk}^{(\alpha)}(t)|^2 . \tag{37}$$

The total energy deviation is computed from Eq. (30) by subtracting the total energy at the initial time.

Figure 3 shows the excited state population (lower panel), the coherences (middle panel) and the total energy deviation (upper panel) for BMA obtained from CTMQC, CTMQC-E, SH-EDC and QD calculations. CTMQC-E and especially CTMQC both closely follow the exact S_1 population decay up to 6 fs and subsequent back-transfer from around 15 to 20 fs for a later decay from 20 to 24 fs. SH-EDC underestimates the repopulation of S_1 that starts at 15 fs. In terms of coherences all 3 trajectory-based methods predict the right trend qualitatively with CTMQC being closest to the reference quantum dynamics result. Concerning the total energy, CTMQC-E significantly corrects the violation of energy conservation displayed in the CTMQC calculation, with a small energy increase which is caused by two effects. First, for trajectories for which the denominator in Eq. (34) becomes
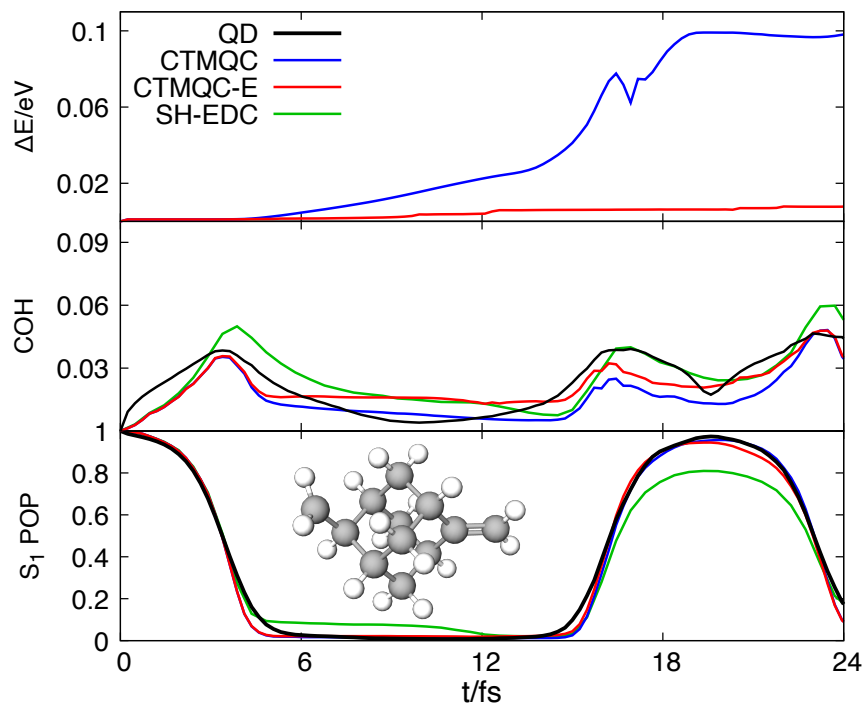
11

FIG. 3. Total energy deviation (upper panel), coherences (middle panel) and excited state populations (lower panel) as a function of time for BMA using CTMQC (blue lines), CTMQC-E (red lines), SH-EDC (green lines) and QD (black lines).

smaller than a fixed threshold, the accumulated force reverts to its original definition, which does not conserve energy. Second, even when the new definition is used, the quantum momentum computation may revert to the original quantum momentum $\mathbf{Q}_0$ definition when a denominator involved in imposing Eq. (21) becomes too small[17,43]: our redefined force is guaranteed to conserve energy only when used in conjunction with the modified definition $\mathbf{Q}_m$.

Although the electronic populations and coherences may be a little worse with CTMQC-E than in CTMQC, the violation of energy conservation of the latter adversely affects the nuclear dynamics. This can be seen in the distribution of classical-like trajectories plotted together with the quantum nuclear density in Figure 4. We observe at 20 fs that the position of some CTMQC trajectories diverge from the nuclear density exploring regions of large negative values of the x-coordinate, as a consequence of an increase in the total energy of the ensemble. Applying the correction to the accumulated force in CTMQC-E remarkably improves energy conservation and the trajectories follow closely the exact density.

Let us now focus on the results for the butatriene cation in Figure 5. We observe that all trajectory-based methods underestimate the rapid S_1 population decay up to 20 fs. Interestingly, SH-EDC is the best performing method. CTMQC underestimates the initial population transfer event prior to 10 fs, and overestimates both the back-transfer at about 12 fs and a subsequent transfer around 20 fs. CTMQC-E on the other hand underestimates the initial population transfer but the subsequent two transfer events follow the trend of the exact
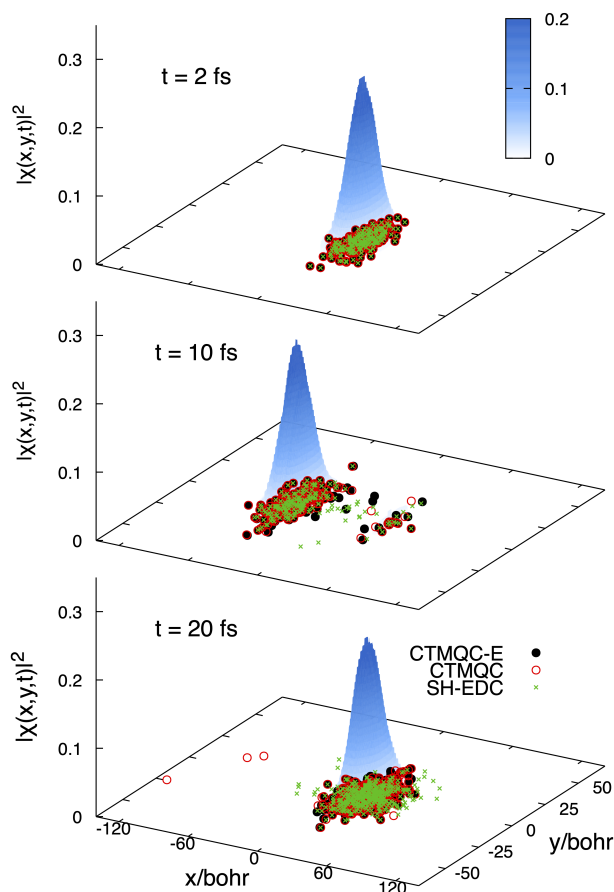
12

FIG. 4. Snapshots of the nuclear density and distribution of trajectories for BMA.

more closely (the populations are shifted up due to the initial underestimate). Interestingly, all the trajectory-based methods miss the repopulation of the excited state at 36 fs. In terms of coherences, CTMQC and SH-EDC predict the QD trend with a decay in the coherence after the passage through the CI rising later at around 40 fs. CTMQC-E on the other hand, remains overcoherent. In terms of energy conservation, CTMQC-E improves energy conservation reducing the energy leakage of CTMQC, which impacts the nuclear dynamics. Figure 6 shows the trajectory-averaged values of the nuclear coordinates as a function of time and the QD expectation values together with their corresponding variances. We observe that all trajectory-based methods capture the dynamics along x. In terms of the variance σ_x all the trajectory-based methods show similar behavior up to 10 fs differing from the QD reference when the wavepacket funnels through the CI. CTMQC starts clearly deviating from the QD reference trend at 10 fs, growing rapidly due to a gain of the total energy of the ensemble. CTMQC-E corrects the behavior and shows similar variance than SH-EDC and both slightly over-dampen the oscillations on σ_x. The increase in the total energy of the ensemble is manifested also in the dynamics along y. We observe that in CTMQC the average value of y deviates significantly from the QD reference showing a very large positive oscillation. CTMQC-E on the other hand overcompensates this behavior showing reduced oscillation on
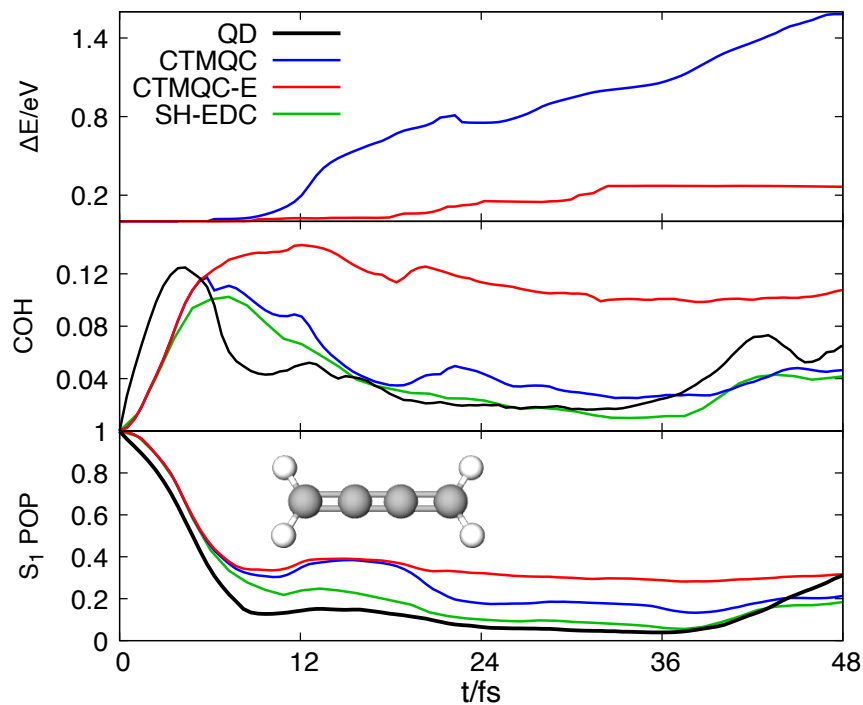
13

FIG. 5. Total energy deviation (upper panel), coherences (middle panel) and excited state populations (lower panel) as a function of time for butatriene cation using CTMQC (blue lines), CTMQC-E (red lines), SH-EDC (green lines) and QD (black lines).
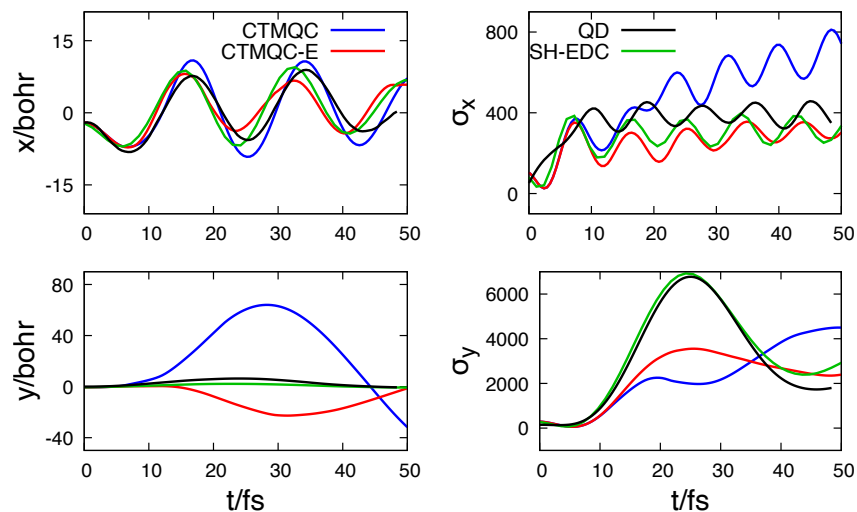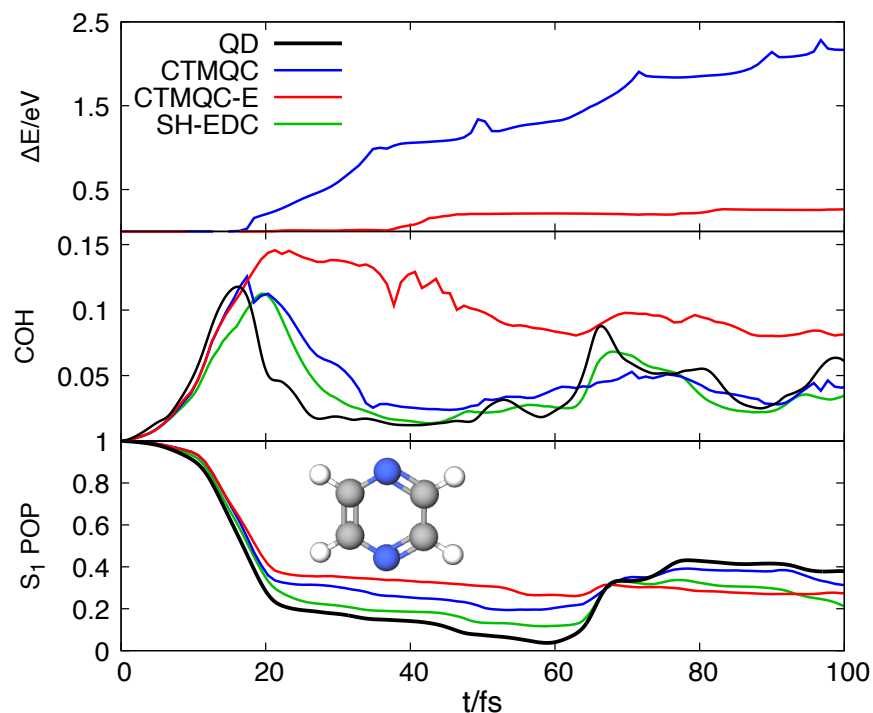

FIG. 6. Average values of the nuclear positions (upper panels) and corresponding variances (lower panel) for butatriene using CTMQC (blue lines), CTMQC-E (red lines), SH-EDC (green lines) and QD (black lines).

the opposite direction, while SH-EDC matches pretty well the QD reference in terms of both

14

FIG. 7. Total energy deviation (upper panel), coherences (middle panel) and excited state populations (lower panel) as a function of time for pyrazine using CTMQC (blue lines), CTMQC-E (red lines), SH-EDC (green lines) and QD (black lines).

y and its varaince σ_y. CTMQC-E shows reduced increase in the variance, while CTMQC underestimates it more initially before then showing an increase later on at 45fs. The CT contribution to the force on the nuclei appears to be responsible for the incorrect behavior in the y-coordinate, since this does not occur for CTTSH (not shown here).

Finally, let us take a look at the case of the pyrazine model. The populations, coherences and total energy deviation are shown in Figure 7. As in the previous case for the butatriene cation, all methods underestimate the first initial population decay, with SH-EDC outpeforming CTMQC and CTMQC-E with a population behaviour similar to the QD results. In terms of coherences, SH-EDC simulates the decoherence and recoherence closely, and CTMQC captures the decoherence well but shows a more gradual recoherence than the exact. CTMQC-E, on the other hand, remains overcoherent. The increase in the total energy of the system is notably reduced with the accumulated force correction of CTMQC-E as evidenced in the lower panel.

In summary, for these models we observe that the quality of the dynamics is improved in terms of nuclear properties, while the electronic, are either slightly improved by CTMQC-E in comparison to CTMQC or remain not very much affected by the correction. Nonetheless, such a correction affect sometimes the coherences, which is a probably fair price to pay since the overall dynamics is stabilized by reducing the energy drift observed in CTMQC.

15

B. Ultrafast photoisomerization of PSB3

Our second example is a 3-dimensional two-state model[58] of the photo-induced isomerization of PSB3, which has been studied in Ref. [45,59] with various trajectory-based methods as well as in Ref. [35] with CTMQC-E. Here, we will extend the analysis on the mechanism of action of CTMQC-E and the consequences for some nuclear observables.
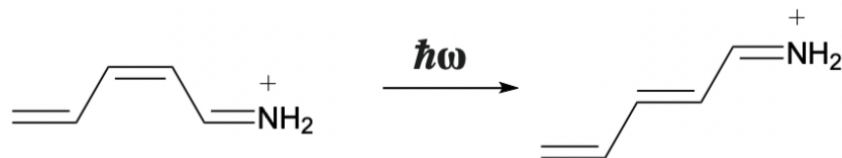

FIG. 8. Schematic representation of isomerization process of PSB3.

The diabatic Hamiltonian is

$$H_{BO}(r,\theta,\phi) = \begin{pmatrix} V_1(r,\theta,\phi) & \lambda(\theta,\phi) \\ \lambda(\theta,\phi) & V_2(r,\theta,\phi) \end{pmatrix} \tag{38}$$

The nuclear degrees of freedom $\underline{\mathbf{R}} = (r,\theta,\phi)$, are the bond-length-alternation stretching (r), the torsional deformation around the double reactive bond C=C (θ) and the hydrogen-out-of-plane wagging (ϕ). These modes drive the ultrafast isomerization of PSB3 after photo-excitation to the first singlet excited state (S_1)[60,61]. The expression for the diabatic potentials and couplings can be found in Appendix A 2.

In our trajectory simulations, we propagated $N_{tr} = 600$ Wigner-distributed trajectories starting in the S_1 state, with centers at $(0.172459 \, \mathrm{bohr}, 0°, 0°)$ for the r, θ and ϕ coordinates, all with zero center momentum. The variances were $(0.154449 \, \mathrm{bohr}, 0.183302°, 0.406143°)$. Periodic boundary conditions were applied to the θ and ϕ degrees of freedom, with periodicities of 2π and 4π, respectively. The same periodicity was imposed on the centers of the quantum momentum. We used a nuclear and electronic time-step of $dt = 0.00024$ fs $(0.01\hbar/\mathrm{Ha})$. For the QD simulations, the initial wavepacket is propagated with a time-step of 1 fs in the diabatic representation with the short iterative Lanczos approach[62,63] implemented in ElVibRot.[64] Furthermore, the wavepacket is expanded on the same basis sets as the ones used in Ref [45].

Figure 9 shows the excited state population decay and the total energy deviation for PSB3. All methods overestimate the initial population transfer to S_0, and tend to incorrectly plateau around 90 fs for some time before subsequently continuing to transfer. After about 120 fs, the trend in CTMQC-E is close to the exact, giving a small improvement over CTMQC and SH-EDC. In terms of total energy, CTMQC-E reduces the total energy violation of CTMQC with some energy drift after 90 fs due to the numerical implementation as discussed in Sec. III when considering the results for BMA.

In our previous work[35] we showed how CTMQC-E correctly captures the kinetic energy along r, whose average increases in a monotonic way due to the wavepacket moving through the CI towards S_0, while its oscillations decrease in amplitude as a result of a loss in vibrational coherence as the wavepacket spreads along θ[45]. There we showed that, while CTMQC
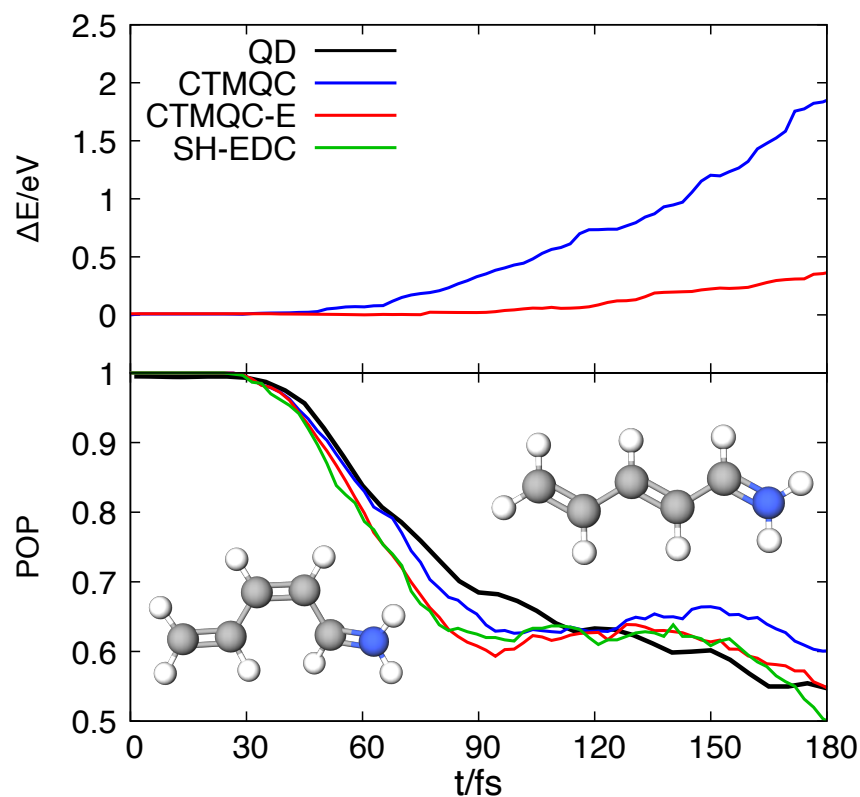
16

FIG. 9. Total energy deviation (upper panel) and excited state populations (lower panel) as a function of time for PSB3 using CTMQC (blue lines), CTMQC-E (red lines), SH-EDC (green lines) and QD (black lines).

captures the initial behavior, it starts to deviate from the exact reference at around 80 fs. The lower panel of Figure 10 shows the value of the momentum along the r coordinate (P_r) and the upper panel the corresponding variance (σ_{P_r}). We observe that all methods follow the trend of the expectation value of the momentum along r with SH-EDC slightly overdamping the oscillations around the average value towards the end of the simulated dynamics with respect to CTMQC, CTMQC-E and the QD reference. Despite this observable agreeing with QD, it is clear that CTMQC deviates from the reference at 90 fs since the variance of the momentum grows rapidly, as expected from the incorrect behavior of the kinetic energy along the r coordinate pointed out in Ref. [35]. With the redefined integrated force of CTMQC-E, this rapid growth is prevented, yielding a variance along r that follows closely the QD reference. To further illustrate this conclusion, we analyze some representative trajectories of the ensemble. Figure 11 shows the values of the position and momenta along r for two trajectories. We observe how in CTMQC the momenta along r starts oscillating with high amplitudes after 150 fs which makes the r coordinate, in turn, fluctuate also far away from its average value. CTMQC-E dampens these oscillations and results in a kinetic energy along r (and a variance of the momentum along r) that matches the QD calculations.
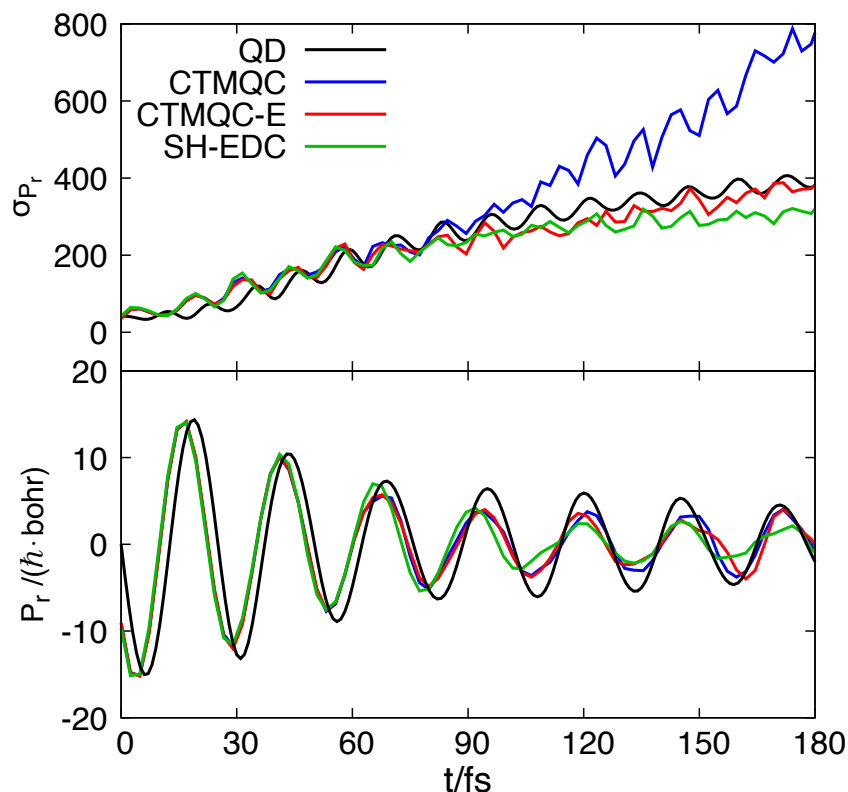
17

FIG. 10. Variance of the momentum along the r coordinate (upper panel) and average value of the momentum along the r coordinate (lower panel) for PSB3.

C. Photo-relaxation dynamics through a 3-state CI: the Uracil cation radical

The last model is an 8-mode linear vibronic coupling (LVC) model with the four lowest lying electronic states (D_0, D_1, D_2, D_3) of the uracil radical cation[65], with diabatic Hamiltonian in terms of the mass-weighted vibrational normal modes $\underline{\underline{\mathbf{R}}} = \mathbf{q}$

$$H_{BO}(\mathbf{q}) = \begin{pmatrix} H_{11}(\mathbf{q}) & \lambda_{12}(\mathbf{q}) & \lambda_{13}(\mathbf{q}) & \lambda_{14}(\mathbf{q}) \\ \lambda_{12}(\mathbf{q}) & H_{22}(\mathbf{q}) & \lambda_{23}(\mathbf{q}) & \lambda_{24}(\mathbf{q}) \\ \lambda_{13}(\mathbf{q}) & \lambda_{23}(\mathbf{q}) & H_{33}(\mathbf{q}) & \lambda_{34}(\mathbf{q}) \\ \lambda_{14}(\mathbf{q}) & \lambda_{24}(\mathbf{q}) & \lambda_{34}(\mathbf{q}) & H_{44}(\mathbf{q}) \end{pmatrix} \tag{39}$$

The analytical expression for the matrix elements in the model is summarized in appendix A 3. The normal modes are 6 modes of A' symmetry ($q_{18}, q_{20}, q_{21}, q_{24}, q_{25}, q_{26}$) and 2 modes of A'' symmetry (q_{10}, q_{12}) within the uracil C_s point group. Modes q_{25} and q_{26} correspond to the two C=O stretches, mode q_{24} correspond to the C=C stretch, modes q_{18}, q_{20} and q_{21} contain CN stretch and NCH/CNH bending motions and q_{10} and q_{12} are out of plane motions. This system, after photoionization to the D_2 excited cationic state, undergoes relaxation to the ground state before fragmentation involving ultrafast dynamics through a
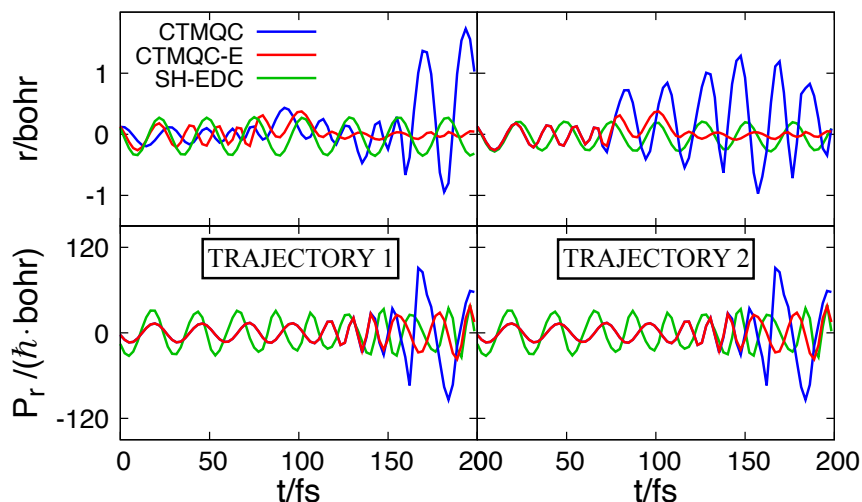
18

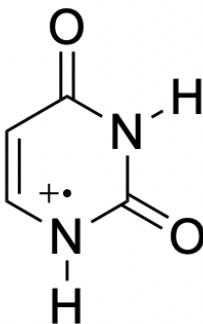FIG. 11. Value of the r coordinate and momentum along the r coordinate for two representative trajectories

FIG. 12. Lewis structure of the Uracil radical cation.

D_0/D_1 and a $D_0/D_1/D_2$ CIs[65,66]. Ref.[34] studied this process, benchmarking against the multiconfigurational time dependent hartree method (MCTDH)[67], with traditional decoherence corrected SH methods and with SHXF, a EF-based SH algorithm where the electronic coefficients evolve according to Eq. (13). It was shown that the extra term in the electronic evolution coming from EF was crucial to capture the dynamics through such multistate intersection through quantum-momentum-driven transitions. We perform SH-EDC, CTMQC and CTMQC-E simulations comparing with MCTDH reference. For the SH-EDC calculations, an ensemble of $N_{tr} = 1000$ trajectories is initialized in an incoherent mixed state described by the density operator $\hat{\rho} = 0.01|D_0\rangle\langle D_0| + 0.05|D_1\rangle\langle D_1| + 0.94|D_2\rangle\langle D_2|$, where 1% of the trajectories are initialized with $\rho_{D_0} = 1$, 5% with $\rho_{D_1} = 1$, and 94% with $\rho_{D_2} = 1$ to match the MCTDH adiabatic populations. For CTMQC(-E) $N_{tr} = 400$ trajectories are run starting in a pure state where each trajectory has initial populations $\rho_{D_0}^{(\alpha)} = 0.01$, $\rho_{D_1}^{(\alpha)} = 0.05$ and $\rho_{D_2}^{(\alpha)} = 0.94$. The initial electronic state used in the MCTDH reference is a pure state at each nuclear configuration, so this is likely a more accurate representation of the initial electronic

state, however, with the assumption that the initial coefficients are real. It has an important effect on the dynamics: the quantum momentum is active from the start, in a region where the wavepackets overlap. The time-step used in the calculations is 0.25 fs for SH-EDC and 0.001 fs ($0.04\hbar/\text{Ha}$) for the coupled-trajectory schemes. The initial conditions for the nuclear trajectories are obtained via Wigner sampling of the neutral uracil ground state (S_0) at the equilibrium geometry with variances obtained from the frequencies of the eight modes in the model.

Figure 13 shows the electronic populations and total energy deviation as a function of time computed with SH-EDC, CTMQC and CTMQC-E, along with the MCTDH benchmark extracted from Ref. [65]. We observe that SH-EDC largely underestimates the rate of population transfer from D_2 to D_0 and cannot describe the fast initial decay of the D_0 population. Instead, CTMQC captures the initial decay very accurately, following the MCTDH populations very closely up until 30 fs. Afterwards, it slightly deviates from the MCTDH reference and plateaus before continuing to decrease at the same rate. Overall the D_2 to D_0 population transfer is underestimated and some population is transferred to the high energy D_3 state, not observed in MCTDH or SH-EDC. Applying the energy correction in CTMQC-E yields worse population behavior than CTMQC, underestimating the D_2 to D_0 transfer and provides a relatively small improvement over SH-EDC. Nonetheless, the top panel of Figure 13 confirms that the drift in total energy observed in CTMQC is reduced in CTMQC-E. As in the other cases, we see that the improved energy conservation improves the nuclear observables: in Figure 14 we plot the values of the C-N, C=O and C=C bond lengths as a function of time obtained with CTMQC, CTMQC-E and SH-EDC, together with the MCTDH reference values. These bonds are related to the important modes included in the linear vibronic coupling model. In some cases, e.g., for the C=N and C=O bonds, after around 20 fs CTMQC deviates from the MCTDH reference predicting oscillations with larger amplitudes, reminiscent of our observations reported for the bond-length-alternation coordinate in PSB3. The energy correction in CTMQC-E reduces the oscillations and yields better energy conservation.

IV.   CONCLUSIONS

We reported an extensive analysis of the performance of the CTMQC-E algorithm for electron-nuclear non-adiabatic dynamics, an exact-factorization-based approach recently designed to mitigate the deviation from the conservation of total energy of CTMQC.

While the original coupled-trajectory algorithm derived from the exact-factorization, i.e., CTMQC, was derived from first-principles, the approximations introduced result in some exact conditions not being guaranteed. In a similar spirit to the fix made in CTMQC to ensure the physical condition of zero trajectory-averaged electronic population transfer when the NAC between pairs of states is zero, CTMQC-E was proposed[35] as a fix on CTMQC to ensure energy conservation over the trajectory ensemble, extending an idea proposed for independent trajectories in Ref. [41]. Correcting the trajectory-averaged energy may have a significant effect on general observables of the system, nuclear and electronic, and our results here have explored this over a range of systems where the electronic and nuclear dynamics are strongly and non-trivially coupled after a photo-excitation.
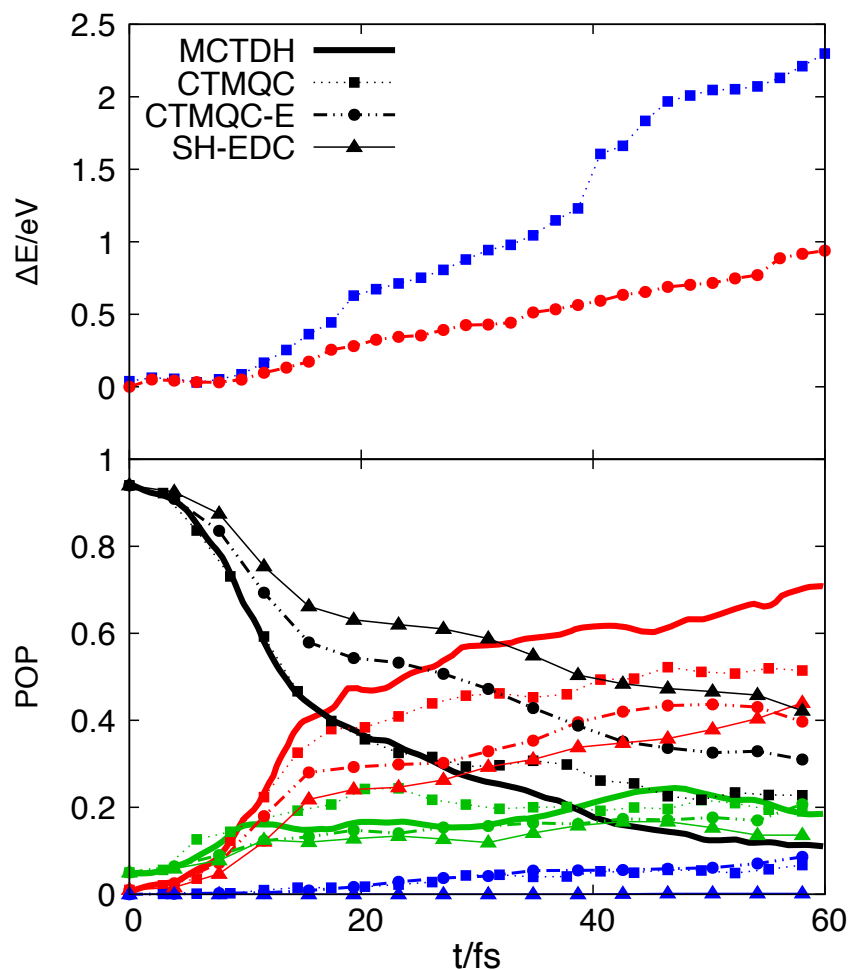
20

FIG. 13. Total energy deviation (upper panel) and electronic populations (lower panel) of the ground D_0 state (red), D_1 (green), D_2 (black) and D_3 (blue) states as a function of time for the Uracil radical cation with MCTDH (bold lines), CTMQC (squares) and CTMQC-E (circles) and SH-EDC (triangles).

In this work, we used the G-CTMQC[52] code to compare CTMQC-E with CTMQC and with surface hopping (with energy decoherence corrections) as well as to validate the accuracy of the correction towards energy conservation. We employed several molecular models that offer a broad test-bed for CTMQC-E, involving two-state or three-state conical intersections, two, three and eight (with 36 Cartesian coordinates) vibrational modes, and with and without periodic boundary conditions. In all cases, CTMQC-E efficiently improves energy conservation with respect to CTMQC, thus allowing us to expect stabilization of the dynamics at long times, particularly for the nuclear observables. In some cases, however, electronic observables are affected in such a way that they deviate from the CTMQC and from the reference, suggesting that there is still room for improvements and novel developments. Future work includes, for example, using other directions for the redefined accumulated force in CTMQC-E to ensure energy conservation, and the possibility of tuning the CTMQC-E correction only
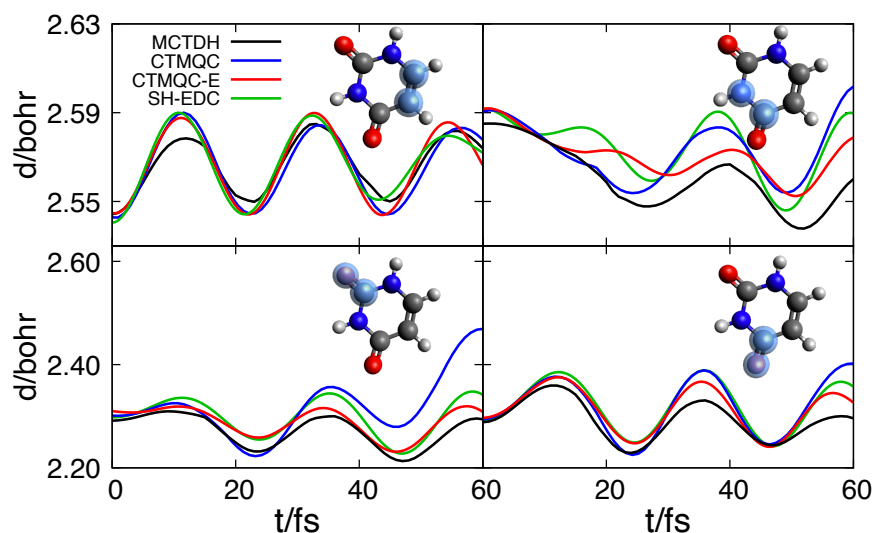
21

FIG. 14. Uracil cation bond lengths as a function of time for the C=C (top left), C-N (top right) and C=O bonds (bottom panels) using CTMQC (blue lines), CTMQC-E (red lines), SH-EDC (green lines) and MTCTDH (black lines).

in certain ranges of energy deviations, while using the original CTMQC when the total energy is well-behaved.

V. ACKNOWLEDGEMENTS

22

Appendix A: Appendix

1. Analytical Potentials for 2D-CI Models

The matrix elements of the diabatic potential energy matrix are

$$V_1(x, y) = \frac{\omega_1^2}{2}\left(x + \frac{a}{2}\right)^2 + \frac{\omega_2^2}{2}y^2 + \frac{\Delta}{2}$$

$$V_2(x, y) = \frac{\omega_1^2}{2}\left(x - \frac{a}{2}\right)^2 + \frac{\omega_2^2}{2}y^2 - \frac{\Delta}{2}$$

$$\lambda(y) = cy \tag{A1}$$

Where the parameters for BMA, butatriene and pyrazine are summarized in Table II.

	$\omega_1 \cdot 10^{-3}$	$\omega_2 \cdot 10^{-3}$	a	$c \cdot 10^{-5}$	$\Delta \cdot 10^{-2}$
BMA	7.743	6.680	31.05	8.092	0
Butatriene	9.557	3.3515	20.07	61.27	1.984
Pyrazine	3.650	4.186	48.45	49.46	2.757

TABLE II. Parameters for BMA, butatriene and pyrazine models. ω_1 and ω_2 are given in $\mathrm{Ha}^{1/2}$/bohr x and y in bohr, c in Ha/bohr and Δ in Ha.

2. Analytical Potentials for PSB3

For PSB3 the diabatic potentials and couplings are

$$V_1(r, \theta, \phi) = H_{cov2D}(r, \theta, \phi) + H_{corr}(\phi)$$

$$V_2(r, \theta, \phi) = H_{ct2D}(r, \theta, \phi) + H_{corr}(\phi)$$

$$\lambda(\theta, \phi) = k_1 sin(2\theta - \phi) \tag{A2}$$

Where

$$V_1(r, \theta, \phi) = \left(V_{Morse_1}(r) + d_2\right) sin^2\left(\theta - \frac{\phi}{2}\right)$$

$$+ d_3 cos^2\left(\frac{\theta}{2} - \frac{\phi}{4}\right) + V_{Morse_2}(r) cos^2\left(\theta - \frac{\phi}{2}\right)$$

$$+ h_1 sin^2\left(\frac{\phi}{4}\right)$$

$$V_2(r, \theta, \phi) = \left(1 + c_5 sin^2(\theta)\right)\left(c_1 r^2 + c_2 r + c_3\right) + c_4 cos(\theta)$$

$$+ h_1 sin^2\left(\frac{\phi}{4}\right) \tag{A3}$$

Being the Morse potentials

$$V_{Morse_1}(r) = d_r \left(e^{-d_1(r - r_{TS})} - 1\right)^2$$

$$V_{Morse_2}(r) = d_r \left(e^{-d_4(r - r_{min})} - 1\right)^2 \tag{A4}$$

The values for the parameters are summarized in the following table

23

	H_{cov2D}	H_{corr}	H_{cp}
h_1		155.7	
k_1			24.04
kf_1	3733		
d_2	54.63		
d_3	3.801		
kf_4	1097		
d_r	2000		
r_{TS}	0.02508		
r_{min}	0.09126		

TABLE III. Parameters for the PSB3 model. h_1 and k_1 are given in kcal/mol, d_2, d_3, and d_r in kcal/(mol·Å), kf_1 and kf_4 in kcal/(mol·Å^2), and r_{min} and r_{TS} in Å.

3. Analytical Potentials for Uracil radical cation

For the uracil cation the diabatic potentials and couplings have the following form

$$V_i(\mathbf{q}) = E_i + \sum_{\nu} \left(f_i(q_\nu) + \kappa_i^{(\nu)} q_\nu + \frac{1}{2} \gamma_i^{(\nu)} q_\nu^2 + \frac{1}{24} k_i^{(\nu)} q_\nu^4 \right)$$

$$\lambda_{ij}(\mathbf{q}) = \sum_{\nu} \lambda_{ij}^{(\nu)} q_\nu \qquad \text{(A5)}$$

where $\{q_\nu\}$ are the mass-frequency-scaled normal coordinates related to the cartesian coordinates $\{R_\nu\}$ via

$$q_\nu = \sqrt{\omega_\nu} \sum_{\mu} K_{\mu\nu} \sqrt{M_\mu} \left(R_\mu - R_{0,\mu} \right) \qquad \text{(A6)}$$

with K denoting the orthogonal cartesian-to-normal modes conversion matrix and $\{R_{0,\nu}\}$ the cartesian coordinates at the reference geometry. $\{E_i\}$ are the electronic state energies at a reference geometry $\mathbf{q} = \mathbf{q_0}$ and $f_i(q_\nu)$ is a harmonic function for modes 10,12,18,20,21 and a Morse function for modes 24,25,26

$$f_i(q_\nu) = \begin{cases} \frac{\omega_\nu}{2} q_\nu^2 & \nu = 10, 12, 18, 20, 21 \\ d^{(\nu)} \left(e^{a_i^{(\nu)}(q_\nu - \sigma_i^{(\nu)})} - 1 \right)^2 + \eta_i^{(\nu)} & \nu = 24, 25, 26 \end{cases} \qquad \text{(A7)}$$

REFERENCES

[1] E. Romero, V. I. Novoderezhkin, and R. van Grondelle, Nature **543**, 355 (2017).
[2] E. Tapavicza, A. M. Meyer, and F. Furche, Phys. Chem. Chem. Phys. **13**, 20986 (2011).
[3] G. D. Scholes, G. R. Fleming, L. X. Chen, A. Aspuru-Guzik, A. Buchleitner, D. F. Coker, G. S. Engel, R. van Grondelle, A. Ishizaki, D. M. Jonas, J. S. Lundeen, J. K. McCusker, S. Mukamel, J. P. Ogilvie, A. Olaya-Castro, M. A. Ratner, F. C. Spano, K. B. Whaley, and X. Zhu, Nature **543**, 647 (2017).
[4] H. Satzger *et al.*, Proc. Natl. Acad. Sci. U.S.A. **103**, 10196 (2006).

	q_{10}	q_{12}	q_{18}	q_{20}	q_{21}	q_{24}	q_{25}	q_{26}
ω	734	771	1193	1383	1406	1673	1761	1794
κ_{D_0}	0	0	-0.02203	-0.12147	-0.09468	0	0	0
κ_{D_1}	0	0	0.09074	0.05316	0.04454	0	0	0
κ_{D_2}	0	0	0.02748	0.11233	0.14539	0	0	0
κ_{D_3}	0	0	-0.04054	0.00747	0.00050	0	0	0
γ_{D_0}	0	0	0.01938	0.01489	0.00970	0	0	0
γ_{D_1}	0	0	0.00694	0.00828	0.00096	0	0	0
γ_{D_2}	0	0	-0.00294	0.00183	-0.00114	0	0	0
γ_{D_3}	0	0	0.00752	0.00546	0.01108	0	0	0
λ_{D_0,D_1}	0.04633	0.03540	0	0	0	0	0	
λ_{D_0,D_2}	0	0	-0.03538	-0.02049	0	0	0.00114	0.13035
λ_{D_1,D_2}	0.03148	0.03607	0	0	0	0	0	0
λ_{D_1,D_3}	0	0	0.08077	0	0.07284	-0.18132	0.12606	0.14272

TABLE IV. Parameters for the uracil model. Frequencies (ω) are given in cm^{-1} and linear terms ($\kappa_i^{(\nu)}$), quadratic terms ($\gamma_i^{(\nu)}$) and coupling parameters ($\lambda_{ij}^{(\nu)}$) in eV.

	q_{24}			
	d	a	σ	η
D_0	41.89704	-0.04719	0.81440	0.81440
D_1	38.37122	-0.05231	0.37488	0.37488
D_2	39.25691	-0.05286	0.14859	0.14859
D_3	37.97847	-0.05431	-0.18152	-0.18152
	q_{25}			
D_0	4.80270	0.13675	0.02883	-0.00007
D_1	74.15995	0.03064	-1.34468	-0.12082
D_2	90.76928	0.03374	-0.29923	-0.00916
D_3	20.56979	0.08044	0.38841	-0.02071
	q_{26}			
D_0	22.92802	-0.07438	-0.32069	-0.01274
D_1	18.27440	-0.07911	-0.01711	-0.00003
D_2	9.46894	-0.08653	0.37635	-0.01037
D_3	65.09678	-0.03660	1.66312	-0.25639

TABLE V. Morse parameters for the uracil model. d and η_i are given in eV, and σ and a are dimensionless.

[5] J. González-Vázquez, L. González, E. Samoylova, and T. Schultz, Phys. Chem. Chem. Phys. **11**, 3927 (2009).

[6] M. Richter, P. Marquetand, J. González-Vázquez, I. Sola, and L. González, J. Phys. Chem. Lett. **3**, 3090 (2012).

[7] A. V. Akimov and O. V. Prezhdo, *Journal of the American Chemical Society*, J. Am. Chem. Soc. **136**, 1599 (2014).

[8] A. A. Chistyakov, M. A. Zvaigzne, V. R. Nikitenko, A. R. Tameev, I. L. Martynov, and O. V. Prezhdo, J. Phys. Chem. Lett. **8**, 4129 (2017).

[9] S. Nah, B. Spokoyny, C. Stoumpos, C. M. M. Soe, M. Kanatzidis, and E. Harel, Nature Photonics **11**, 285 (2017).

[10] M. Born and R. Oppenheimer, Annalen der Physik **389**, 457 (1927).

[11] U. Raucci, H. Weir, S. Sakshuwong, S. Seritan, C. B. Hicks, F. Vannucci, F. Rea, and T. J. Martínez, Ann. Rev. Phys. Chem. **74**, 313 (2023).

[12] A. D. McLachlan, Mol. Phys. **8**, 39 (1964).

[13] J. C. Tully, J. Chem. Phys. **93**, 1061 (1990).

[14] G. Tao, J. Chem. Phys. **144** (2016).

[15] S. K. Min, F. Agostini, and E. K. U. Gross, Phys. Rev. Lett. **115**, 073001 (2015).

[16] F. Agostini, S. K. Min, A. Abedi, and E. K. U. Gross, J. Chem. Theory Comput. **12**, 2127 (2016).

[17] S. K. Min, F. Agostini, I. Tavernelli, and E. K. U. Gross, J. Phys. Chem. Lett. **8**, 3048 (2017).

[18] J.-K. Ha, I. S. Lee, and S. K. Min, J. Phys. Chem. Lett. **9**, 1097 (2018).

[19] C. C. Martens and J.-Y. Fang, J. Chem. Phys. **106**, 4918 (1997).

[20] A. Donoso and C. C. Martens, J Chem. Phys. **112**, 3980 (2000).

[21] A. Donoso and C. C. Martens, Int. J. of Quantum Chem. **90**, 1348 (2002).

[22] C. C. Martens, J. Phys. Chem. Lett. **7**, 2610 (2016).

[23] R. Kapral and G. Ciccotti, J. Chem.Phys. **110**, 8916 (1999).

[24] J. C. Tully, Faraday Discuss. **110**, 407 (1998).

[25] G. Hunter, Int. J. Quantum Chem. **9**, 237 (1975).

[26] G. Hunter, Int. J. Quantum Chem. **9**, 311 (1975).

[27] G. Hunter, Int. J. Quantum Chem. **9**, 133 (1980).

[28] G. Hunter, Int. J. Quantum Chem. **19**, 755 (1981).

[29] G. Hunter and C. C. Tai, Int. J. Quantum Chem. **21**, 1041 (1982).

[30] N. I. Gidopoulos and E. K. U. Gross, Philosophical Transactions of the Royal Society of London A: Mathematical, Physical and Engineering Sciences **372** (2014).

[31] A. Abedi, N. T. Maitra, and E. K. U. Gross, Phys. Rev. Lett. **105**, 123002 (2010).

[32] A. Abedi, N. T. Maitra, and E. K. U. Gross, J. Chem. Phys. **137**, 22A530 (2012).

[33] F. Agostini and E. K. U. Gross, Eur. Phys. J. B **94**, 179 (2021).

[34] P. Vindel-Zandbergen, S. Matsika, and N. T. Maitra, The Journal of Physical Chemistry Letters **13**, 1785 (2022), pMID: 35170972, https://doi.org/10.1021/acs.jpclett.1c04132.

[35] E. Villaseco Arribas and N. T. Maitra, J. Chem. Phys. **158** (2023).

[36] R. Requist, F. Tandetzky, and E. K. U. Gross, Phys. Rev. A **93**, 042108 (2016).

[37] C. Li, R. Requist, and E. K. U. Gross, Phys. Rev. Lett. **128**, 113001 (2022).

[38] F. Agostini, A. Abedi, Y. Suzuki, S. K. Min, N. T. Maitra, and E. K. U. Gross, J. Chem. Phys. **142**, 084303 (2015).

[39] F. G. Eich and F. Agostini, J. Chem. Phys. **145**, 054110 (2016).

[40] C. Pieroni and F. Agostini, J. Chem. Theory Comput. **17**, 5969 (2021).

[41] J.-K. Ha and S. K. Min, The Journal of Chemical Physics (in press) **156**, 174109 (2022).

[42] E. V. Arribas, P. Vindel-Zandbergen, S. Roy, and N. T. Maitra, "Different flavors of exact-factorization-based mixed quantum-classical methods for multistate dynamics," (2023), arXiv:2307.11535 [quant-ph].

[43] E. Villaseco Arribas, F. Agostini, and N. T. Maitra, Molecules **27**, 13 (2022).

[44] B. F. E. Curchod, F. Agostini, and I. Tavernelli, Euro. Phys. J. B **91**, 168 (2018).

[45] E. Marsili, M. Olivucci, D. Lauvergnat, and F. Agostini, J. Chem. Theory Comput. **16**, 6032 (2020).

[46] C. Pieroni, E. Marsili, D. Lauvergnat, and F. Agostini, J. Chem. Phys. **154**, 034104 (2021).

[47] F. Talotta, D. Lauvergnat, and F. Agostini, J. Chem. Phys. **156**, 184104 (2022).

[48] A. Carof, S. Giannini, and J. Blumberger, J. Chem. Phys. **147**, 214113 (2017).

[49]M. Barbatti, J. Chem. Theor. Comput. **17**, 3010 (2021).

[50]D. Tang, L. Shen, and W.-h. Fang, Phys. Chem. Chem. Phys. **23**, 13951 (2021).

[51]Note that the second term in parenthesis is the gauge-invariant part of the approximated TDPES in CTMQC.

[52]F. Agostini, E. Marsili, F. Talotta, and E. Villaseco Arribas, "G-CTMQC," (Last accessed June 2023), `https://gitlab.com/agostini.work/g-ctmqcgitlab.com/agostini.work/g-ctmqc`.

[53]I. G. Ryabinkin, L. Joubert-Doriol, and A. F. Izmaylov, J. Chem. Phys. **140** (2014).

[54]L. M. Ibele and B. F. E. Curchod, J Chem. Phys. **155** (2021).

[55]G. Granucci and M. Persico, J. Chem. Phys. **126**, 134114 (2007).

[56]M. Feit, J. Fleck, and A. Steiger, J. Comp. Phys. **47**, 412 (1982).

[57]A. D. Bandrauk and H. Shen, J. Chem. Phys. **99**, 1185 (1993).

[58]E. Marsili, M. H. Farag, X. Yang, L. De Vico, and M. Olivucci, The Journal of Physical Chemistry A **123**, 1710 (2019).

[59]T. I. Kim, J.-K. Ha, and S. K. Min, Topics in Current Chemistry **380**, 8 (2022).

[60]S. Gozem, M. Huntress, I. Schapiro, R. Lindh, A. A. Granovsky, C. Angeli, and M. Olivucci, J. Chem. Theory Comput. **8**, 4069 (2012).

[61]S. Gozem, F. Melaccio, R. Lindh, A. I. Krylov, A. A. Granovsky, C. Angeli, and M. Olivucci, J. Chem. Theory Comput. , 4495 (2013).

[62]T. J. Park and J. C. Light, J. Chem. Phys. **85**, 5870 (1986).

[63]C. Leforestier, R. Bisseling, C. Cerjan, M. Feit, R. Friesner, A. Guldberg, A. Hammerich, G. Jolicard, W. Karrlein, H.-D. Meyer, N. Lipkin, O. Roncero, and R. Kosloff, J. Comp. Phys. **94**, 59 (1991).

[64]D. Lauvergnat, "ElVibRot, a Quantum Dynamics Code," (accessed in June 2023), `https://github.com/lauvergn/ElVibRot`.

[65]M. Assmann, H. Köppel, and S. Matsika, J. Phys. Chem. A **119**, 866 (2015).

[66]M. Assmann, T. Weinacht, and S. Matsika, J. Chem. Phys. **144**, 034301 (2016).

[67]H.-D. Meyer, U. Manthe, and L. Cederbaum, Chem. Phys. Lett. **165**, 73 (1990).

27